



Coastal Road Slope Collapses Behind a Retaining Wall Due to Scour and Erosion

Ryota Tsubokawa, Engineer, KOKEN ENGINEERING, River Department, Sapporo, Japan, e-mail: r.tsubokawa@koken-e.co.jp

Yasunari Iida, Senior Engineer, KOKEN ENGINEERING, River Department, Sapporo, Japan, e-mail: y.iida@koken-e.co.jp

Yuji Ushiwatari, Executive Officer, KOKEN ENGINEERING, Disaster Prevention Facility Department, Sapporo, Japan, e-mail: ushi@koken-e.co.jp

Tatsuya Matsuda, Associate Professor, Toyohashi University of Technology, Toyohashi, Japan, e-mail: matsuda@ace.tut.ac.jp

Masashi Ochi, Associate Professor, National Institute of Technology, Hakodate College, Hakodate, Japan, e-mail: m-ochi@hakodate-ct.ac.jp

Makoto Miyatake, Professor, National Institute of Technology, Hakodate College, Hakodate, Japan, e-mail: miyatake@hakodate-ct.ac.jp

Shinji Sassa, Head of Soil Dynamics Group and Research Director, Port and Airport Research Institute, National Institute of Maritime, Port and Aviation Technology, Yokosuka, Japan, e-mail: sassa@p.mpat.go.jp

ABSTRACT: *The present study investigates the coastal road slope disasters that took place in December 2014 and in November 2021 in Hokkaido, Japan. The coastal disasters represent collapses behind the retaining walls under high wave conditions. The results of the field investigations demonstrate that the extent of the damages was significantly larger in the 2014 disaster than in the 2021 disaster, and this difference was closely related with the presence and absence of overtopping. Based on the estimated offshore waves, a series of hydraulic wave flume experiments were conducted so as to gain insights into the disaster mechanisms. The combined field and experimental results show that the collapses were the consequence of coupled surface erosion, scour, and internal erosion beneath and behind the retaining walls. The overtopping enlarged the extent of the collapses. The paper also discusses an effective countermeasure meant to suppress such coastal road slope disasters behind retaining walls.*

KEYWORDS: coastal road, scour, erosion, internal erosion, cavity, collapse, retaining wall

SITE LOCATION: [Geo-Database](#)

INTRODUCTION

Coastal roads are subjected to the risks of high waves, overtopping, and flows. In the face of global climate change, the frequency of high wave conditions has been increasing along coasts worldwide (Morim et al., 2019), which threatens the safe passage of vehicles and humans. In Japan, the main traffic routes are often located in the immediate vicinity of the coastline. Seasonal wave effects such as typhoons and winter storms have occasionally caused damages to coastal roads owing to scour and erosion. Developing a better understanding of the disaster risks and associated mechanisms is therefore important for the conservation and maintenance of coastal roads. The present study aims to investigate two coastal road disasters that took place on December 2nd, 2014 and on November 23rd, 2021 in Hokkaido, Japan. The novelty of this study lies in the comparison and explanation of the mechanisms of these two disasters involving surface erosion, scour, and internal erosion around coastal road structures. In the paper, the results from the site investigations conducted for the coastal road slope collapses behind the retaining walls are initially described. This is followed by the numerical estimation of wind waves as the external forces which led to the 2014 and 2021 coastal disasters. The results of a series of hydraulic wave flume experiments performed

Submitted: 24 June 2022; Published: 28 December 2022

Reference: Tsubokawa, R., Iida, Y., Ushiwatari, Y., Matsuda, T., Ochi, M., Miyatake, M. and Sassa, S. (2022). Coastal Road Slope Collapses Behind a Retaining Wall Due to Scour and Erosion. *International Journal of Geoenvironmental Engineering Case Histories*, Volume 7, Issue 4, pp. 39-49, doi: 10.4417/IJGCH-07-04-04

based on the estimated offshore waves are then presented and discussed. The results of the field, numerical, and experimental investigations are summarized in the Conclusion.

FIELD SURVEYS OF THE 2014 AND 2021 COASTAL DISASTERS

The 2014 and 2021 disasters took place during the winter storm seasons along the Ohanzaiham coast in Hokkaido, Japan. The sites of the disasters were located at $41^{\circ}47'16.3''\text{N}$, $140^{\circ}04'28.3''\text{E}$ for the 2014 event (Fig. 2 (a), Fig. 5) and at $41^{\circ}46'18.4''\text{N}$, $140^{\circ}04'21.5''\text{E}$ for the 2021 event (Fig. 2 (b), Fig. 5). The measured time histories of the maximum and significant wave heights and the average wave speeds at and around the times of the 2014 and 2021 disasters are shown in Fig. 1. For both disasters, the low-pressure system potentially leading to extreme weather events had caused high wave conditions at the site. In fact, during the 2014 event, the maximum wave height reached 18.07 m, with a maximum significant wave height of 11.41 m under an average wind speed of 19.1 m/s on December 2nd, 2014. During the 2021 event, the maximum wave height reached 8.25 m, with a maximum significant wave height of 5.05 m shortly after recording an average wind speed of 15.9 m/s on November 24th, 2021. Here, the significant wave height is defined as the average height of the highest one-third of all waves, and the maximum wave height denotes the largest measured wave at a given location.

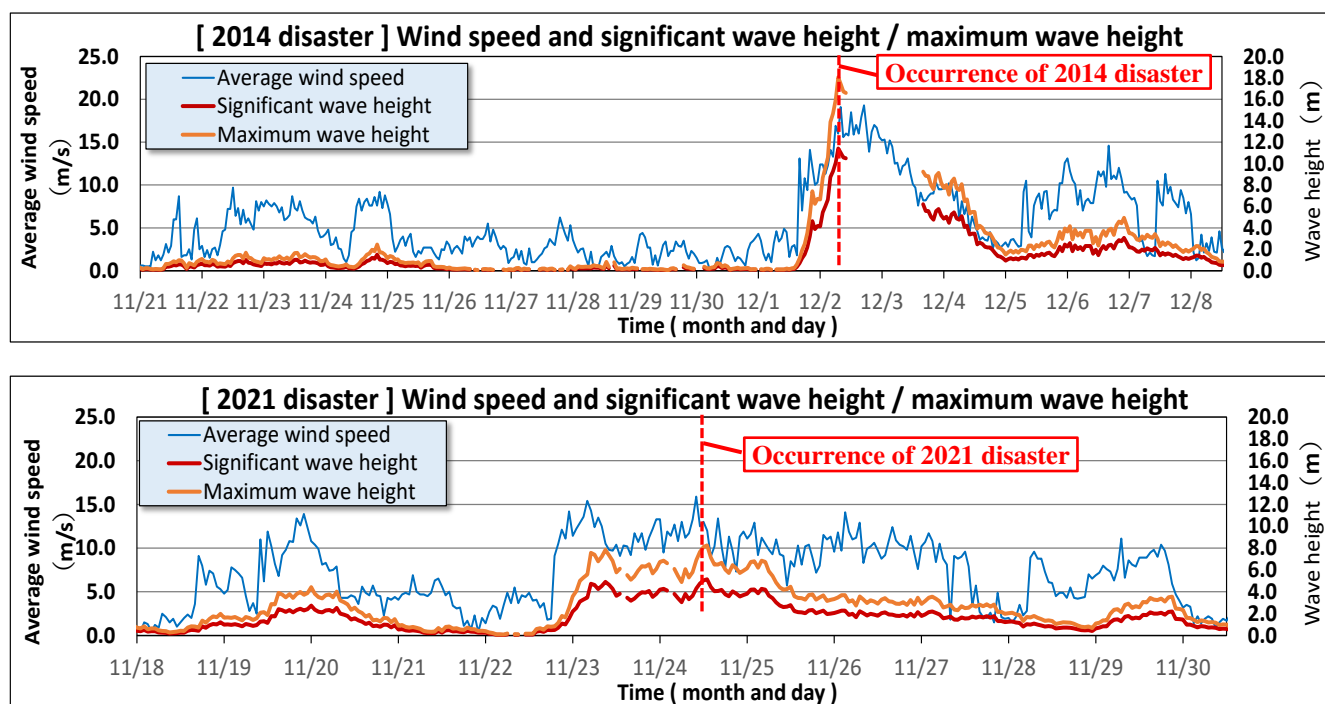


Figure 1. Time histories of significant and maximum wave heights and average wind speeds at/around the times of the 2014 and 2021 disasters.

The results of the field surveys that were conducted several days after the 2014 and 2021 events and in 2019 that corresponded to normal times are shown in Fig. 2. The photographs 2014-I and 2021-I show the situations in 2019 where the foreshores were covered with sand and no significant erosion took place. In contrast, the photographs 2014-II and 2021-II show that the foreshore sands were lost, owing to surface erosion that occurred under the action of high waves; subsequently, the base and foundation of the retaining walls were exposed. At the site of the 2014 event, there existed a weak erodible bedrock beneath sands (2014-II). The photographs 2014-III and 2021-III demonstrate that large collapses took place behind the retaining walls. The extent of collapse during the 2014 event was equal to 8.0 m, which was significantly larger than that of 4.5 m during the 2021 event. The field surveys also identified the trace of peeling of vegetation on the road slope surface behind the retaining wall following the 2014 event, whereas it was not confirmed following the 2021 event. This indicates that the severe wave-induced overtopping flows acted behind the retaining wall at the time of the 2014 event. The associated mechanisms will be discussed later in this paper.



Figure 2. Field surveys of the 2014 and 2021 disasters: (a) Locations of foreshore slope surveys, (b) Situations at normal times (2014-I) and following the 2014 disaster (2014-II, 2014-III), and (c) Situations at normal times (2021-I) and following the 2021 disaster (2021-II, 2021-III).

ANALYSIS OF FORESHORE SLOPES AND WAVES

Foreshore Slopes

The measured results of foreshore slopes are shown in Fig. 3, together with the approximate curve for each profile measurement. The foreshore sand was coarse sand with a median grain diameter $d_{50} = 1.24$ mm. With reference to Fig. 2, the morphological measurements were performed in Sections 1 and 2, which corresponded to the cross-shore transects adjacent to the site of the 2014 disaster, in October 2019, five years after the 2014 event. The morphological measurements were also performed in Section 3, which corresponded to the cross-shore transect just on the site of the 2021 disaster, in September 2021, before the 2021 event. This means that the measurements denote those at normal times. One can see in Fig. 3 that berms were formed near the high-water levels (H.W.L.). While the morphological heights were different from each other, the mean foreshore gradients were essentially the same at 1/10. These results, together with the above field evidence at the times of the disasters, demonstrate that the foreshore sands underwent surface erosion and deposition recurrently, bringing the morphological states into essentially the same foreshore gradients at normal times.

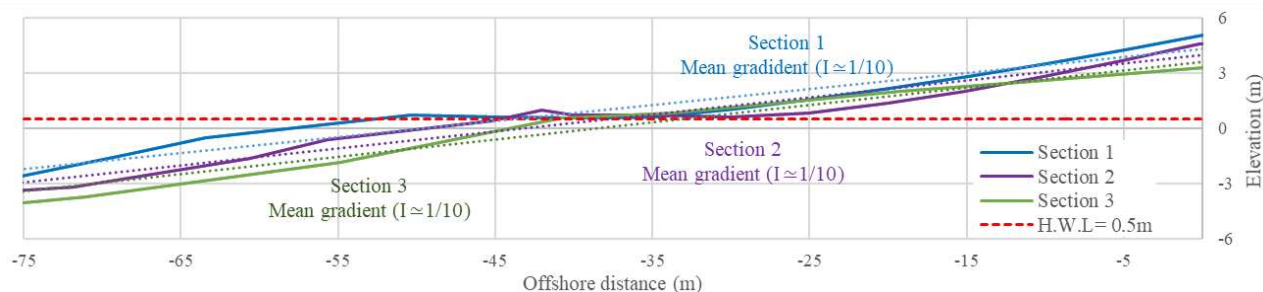


Figure 3. Foreshore slope profiles at normal times. The solid lines represent measured results and the dotted lines denote the approximate curves. Sections 1, 2, and 3 correspond to those shown in Fig. 2(a).

Wave Conditions

The coastal wave maps at the times of the disasters are shown in Fig. 4. For both the 2014 and 2021 disasters, waves were essentially east waves. The fact that the site of the disasters—namely, the coastal road and the foreshores—were located in the north-south direction demonstrates that the waves were propagating essentially orthogonally toward the coast. The wave conditions at the times of the disasters were numerically estimated using a third-generation wave model for coastal regions called SWAN (Simulation Waves Nearshore: Booij et al., 1999; Ris et al., 1999; SWAN Team, 2006). The calculation was conducted based on the input conditions that involved wind speeds, water depths, and bathymetry. The wind information was provided by the Japan Meteorological Agency (Grid Point Value of Meso Scale Model: GPV-MSM), and the water depth/bathymetry data were based on the General Bathymetric Chart of the Oceans (GEBCO, 2020). As the calculation domains (Fig. 5), Domain 1 covered seas surrounding Japan with the longitudes from 120.00° to 149.625° and the latitudes from 22.40° to 49.050°. Domain 2 covered a nationwide region with the longitudes from 127.125° to 143.375° and the latitudes from 33.60° to 47.45°, which included the site of the disasters and the nearby Setana Port. The lattice spacing was 0.1875° in longitude and 0.1500° in latitude for Domain 1, and 0.0625° in longitude and 0.05° in latitude for Domain 2.

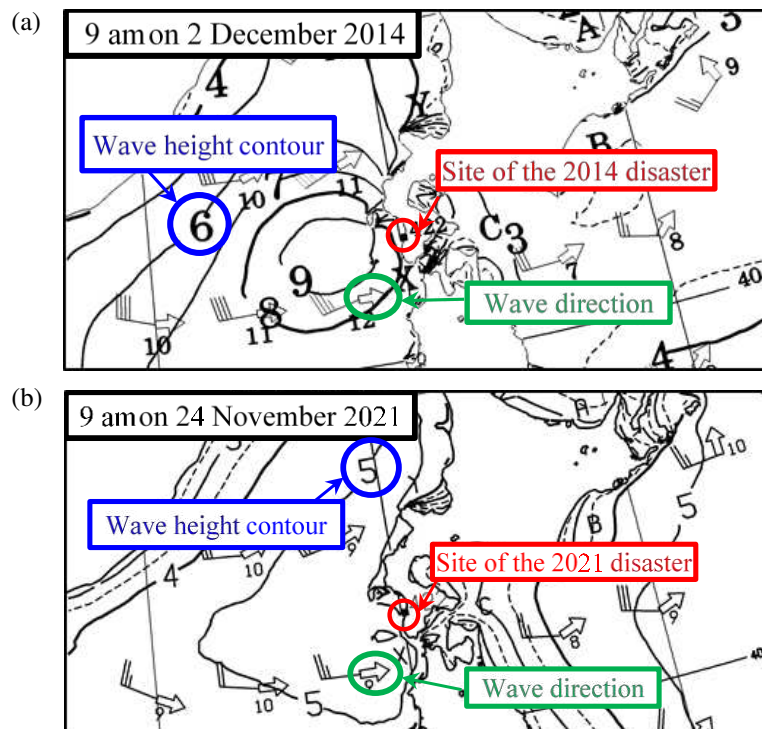


Figure 4. Coastal wave maps at the times of the disasters: (a) December 2014, (b) November 2021.

The calculated significant wave heights and significant wave periods are compared with the measured results off the coast of Setana Port in Fig. 6. The measurements were based on a national wave monitoring system, NOWPHAS (Nationwide Ocean Wave information network for Ports and HARbourS). One can see in Fig. 6 that there is a reasonably good agreement between the results of the calculations and measurements. The calculated and measured significant wave heights and significant wave periods are also well correlated with each other (Fig. 6). Based on the confirmation of the predictive accuracy, the offshore waves for the site of the 2014 disaster were estimated (Fig. 7). It is important here to note that the severe wave conditions at the time of the 2014 disaster resulted in the lack of measurements off the coast near the disaster site. In Fig. 7, a five-year probability wave and a one-year probability wave are also shown for comparison. One can see that the maximum significant wave heights reached over 6 m with the corresponding significant wave periods over 12 s. These values essentially corresponded to the five-year probability wave with the significant wave height $H_{1/3} = 6.7$ m and significant wave period $T_{1/3} = 12.9$ s. The estimated offshore waves for the site of the 2021 disaster are shown in Fig. 8, and are generally in good agreement with the measured results. The 2021 offshore waves wholly corresponded to the one-year probability wave with the significant wave height $H_{1/3} = 4.6$ m and significant wave period $T_{1/3} = 10.7$ s. Overall, the above results indicate that the offshore waves at the time of the 2014 disaster reached the five-year probability wave, whereas the offshore waves at the



time of the 2021 disaster were essentially the one-year probability wave. This information was used for setting the external forces, namely, the input offshore waves for the hydraulic wave flume experiments as described below.

		Domain1	Domain2
Longitude range		120.00°~ 149.625°	127.125°~ 143.375°
Latitude range		22.40°~ 49.050°	33.60°~ 47.45°
Lattice spacing	Longitude	0.1875°	0.0625°
	Latitude	0.1500°	0.05°
External force condition		GPV-MSM (U10 · V10)	

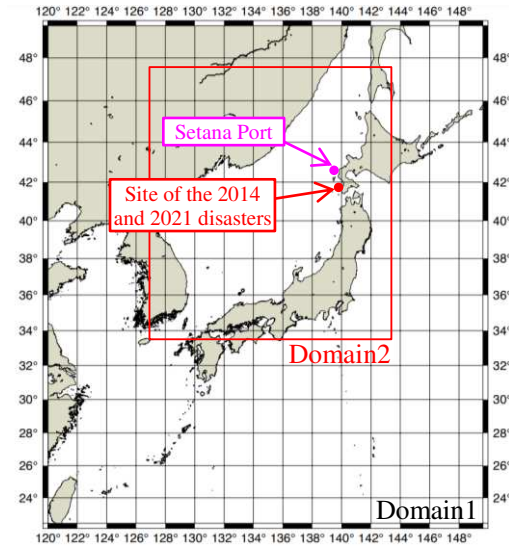


Figure 5. Calculation regions of offshore waves for the 2014 and 2021 disasters using a third-generation wave model (SWAN).

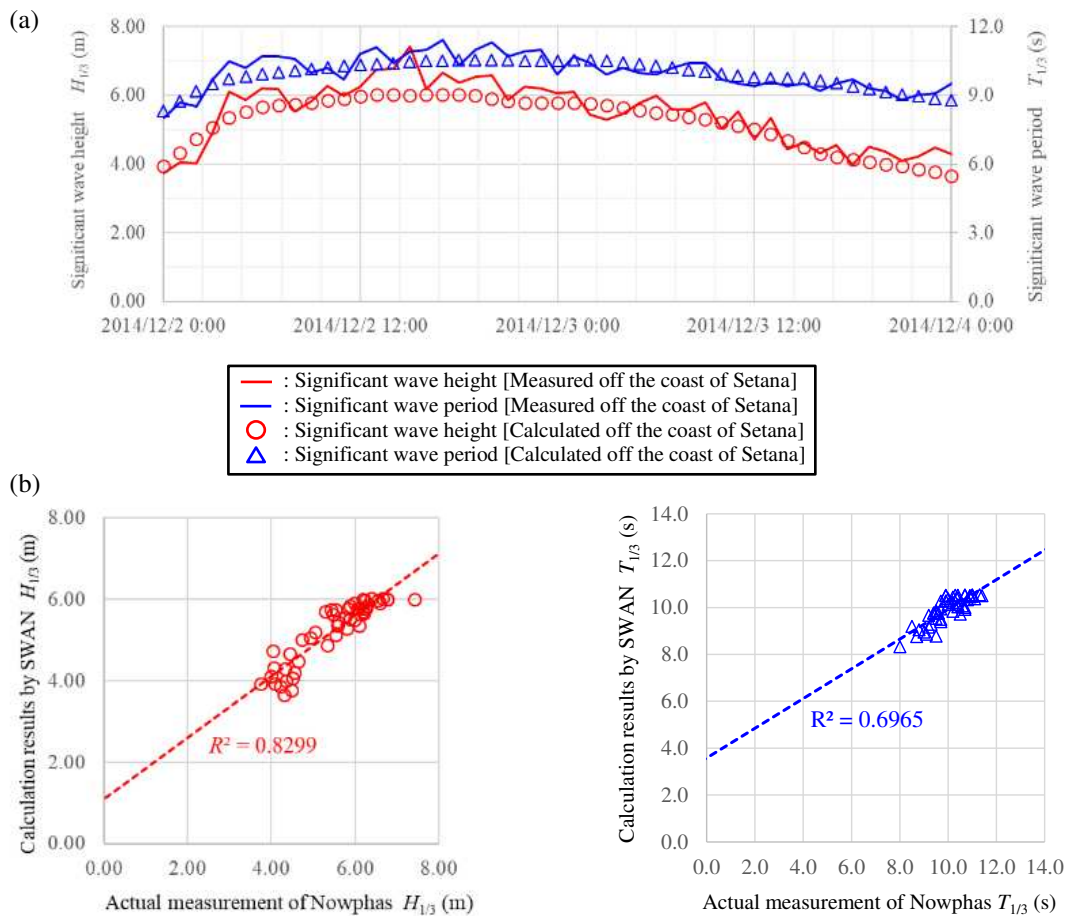


Figure 6. Calculated and measured results of significant wave heights and significant wave periods off the coast of Setana: (a) Time histories, and (b) Correlations.

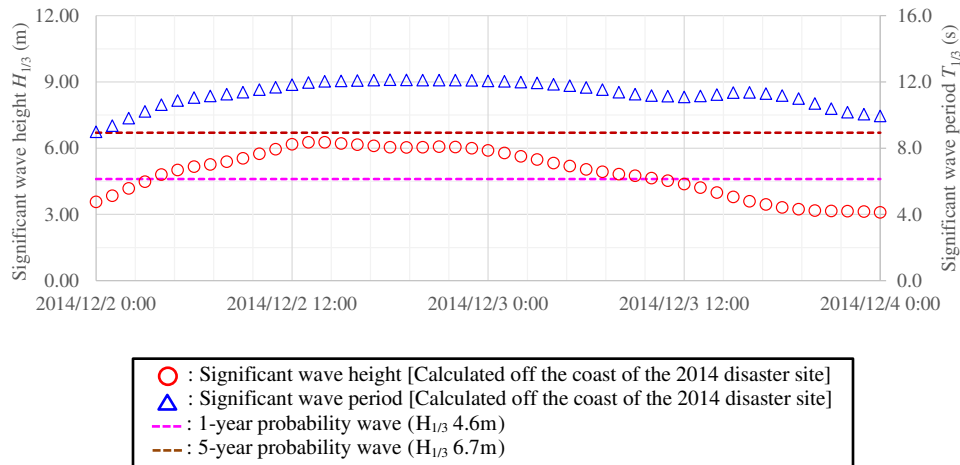


Figure 7. Estimated significant wave heights and significant wave periods off the coast of the 2014 disaster site. The 1-year probability wave and 5-year probability wave are also shown for comparison.

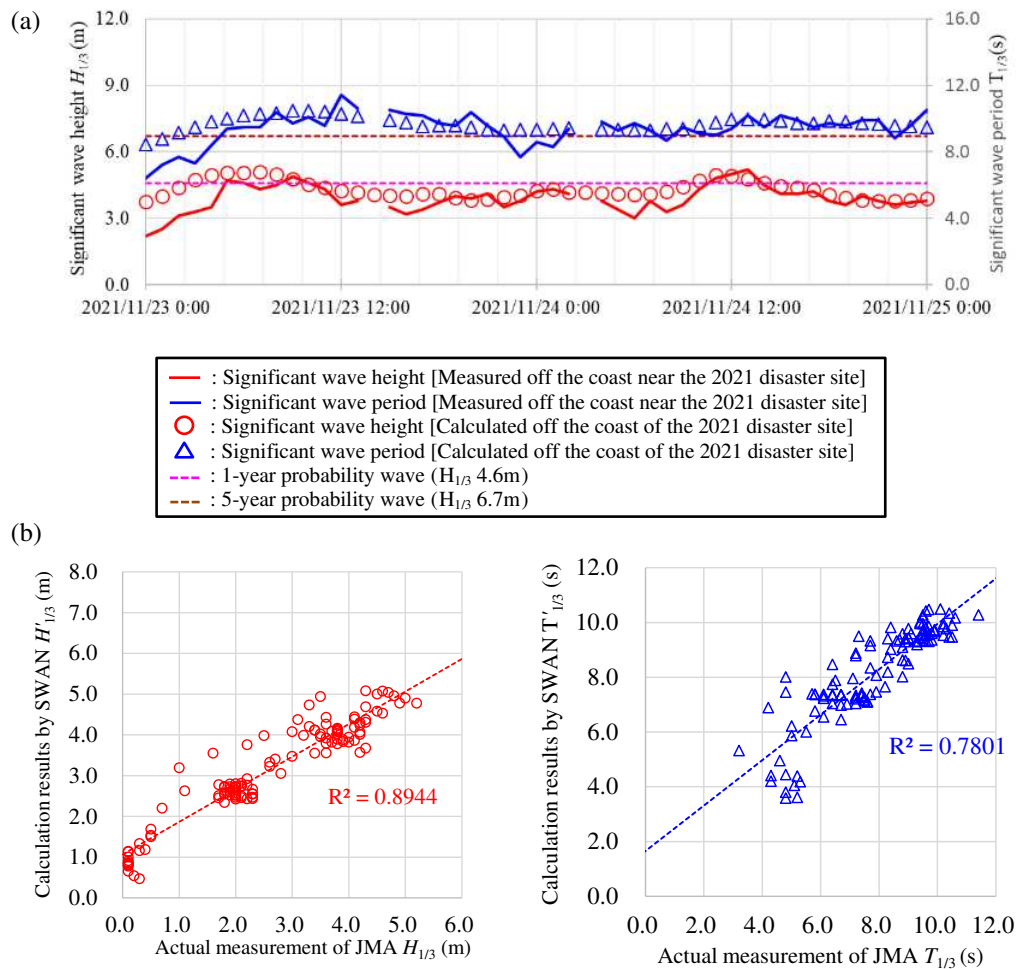


Figure 8. Calculated and measured results of significant wave heights and significant wave periods off the coast of 2021 disaster site: (a) Time histories, and (b) Correlations.

EXPERIMENT ON THE COASTAL ROAD EMBANKMENT SLOPE BEHIND A RETAINING WALL

Material and Method

The experiments were conducted on a two-dimensional cross-section using a wave flume at the National Institute of Technology, Hakodate College, in Hokkaido, Japan. The wave channel is 13.5 m long, 0.9 m high, and 0.5 m wide and has a piston-type wave-maker at the left end of the channel (Fig. 9). The scale of the experiments was 1/50th with reference to the foreshores and retaining walls at the site of the 2014 and 2021 disasters described above. On the basis of the Froude similarity law, the five-year probability wave ($H_{1/3} = 6.7$ m, $T_{1/3} = 12.9$ s) and the one-year probability wave ($H_{1/3} = 4.6$ m, $T_{1/3} = 10.7$ s) were converted to irregular waves with the offshore significant wave heights of 13.4 cm (6.7 m/50) and 9.2 cm (4.6 m/50) and the offshore significant wave periods of 1.82 s ($12.9/\sqrt{50}$) and 1.51 s ($10.7/\sqrt{50}$) respectively, using the Bretschneider-Mitsuyasu (BM) spectrum that is widely known to represent fully-grown wind waves (Bretschneider, 1968; Mitsuyasu, 1970). The coastal bottom slope gradient was set equal to 1/10 and the coastal road slope gradient behind the top of the retaining wall was set equal to 1/2.5 in light of the field. The sand used was silica sand with a median grain diameter $d_{50} = 0.42$ mm. This was determined with reference to the measured permeability coefficient $k_w = 0.038$ cm/s that was $1/\sqrt{50}$ -scale of the measured permeability coefficient $k_w = 0.267$ cm/s of the foreshore sand ($d_{50} = 1.24$ mm) in the field.

It should be noted, however, that the similitudes for wave-soil interactions involving sediment transport and pore water pressures in the soil have not yet been established. Therefore, the purpose of the present experiments was to gain insights into the mechanisms of the 2014 and 2021 disasters. In two series of experiments, the first series targeted the 2014 disaster under the five-year probability wave. The initial condition was such that the base of the retaining wall was already exposed due to surface erosion. The second series targeted the 2021 disaster under the one-year probability wave. The foreshore sand existed at the start of the experiment. The wave-induced flow velocity above the foreshore sand was of the order of 20-30 cm/s, which fell in the bedload regime (Yang et al., 2019). For both series of experiments, sand beds were formed by pouring dry sands and the water levels were set at a high-water level (H.W.L.). Approximately 400 wave cycles corresponding to a duration of 70 minutes on a prototype scale were applied, and the progresses of surface erosion, scour, internal erosion, and collapse were monitored by a digital video camera and analyzed via a digitizer for both series of experiments.

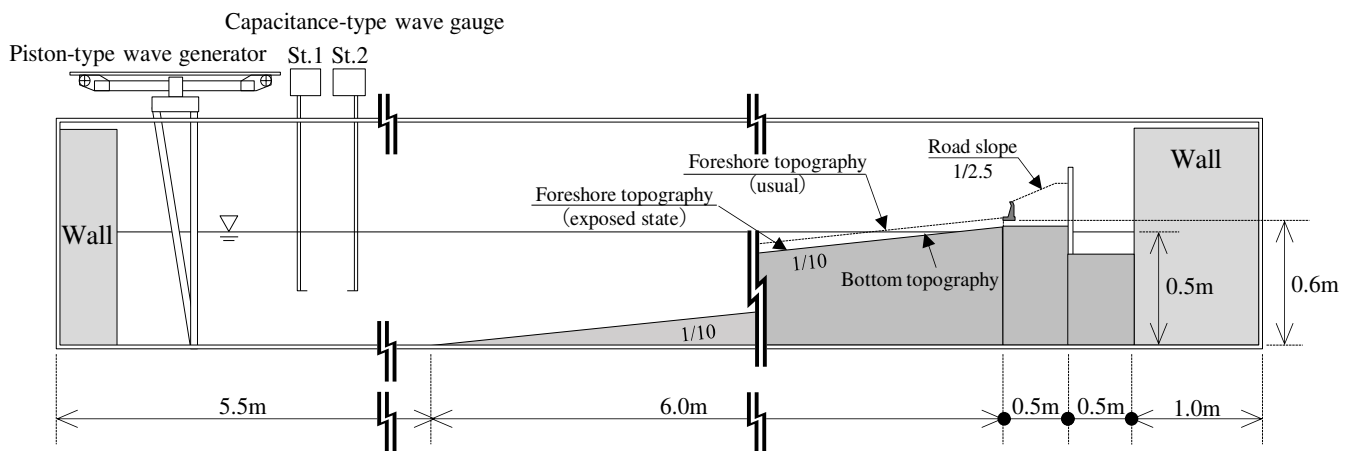


Figure 9. Schematic diagram of a two-dimensional wave flume at National Institute of Technology, Hakodate College, in Hokkaido, Japan, and the experimental setup for the 2014 and 2021 disasters.

Experimental Results

The results of the first series of the wave flume experiment for the 2014 disaster are shown in Fig. 10. At the start of the experiment, the base of the retaining wall was already exposed. The five-year probability wave gave rise to the occurrence of internal erosion beneath the base of the retaining wall. This was accompanied by the formation of a cavity, and the cavity developed towards the back of the retaining wall. Meanwhile, the overtopping induced by the five-year probability wave caused erosion of the slope surface behind the top of the wall. The continued action of the five-year probability wave also resulted in the progress of collapse behind the retaining wall in association with the destabilization of the cavities formed

behind and beneath the retaining wall. The extent of the collapse was equal to 7.5 m on a prototype scale, which was consistent with that of 8 m as a result of the field measurement for the 2014 disaster, as mentioned above. Such progress of internal erosion and collapse beneath and behind the retaining wall can be more directly seen from the photographs shown in Fig. 11. Here, one can see the concurrent cavity occurrence, sand flow, and collapse surrounding the retaining wall.

The results of the second series of the wave flume experiment for the 2021 disaster are shown in Fig. 12. Fig. 12(a) shows deformations as a consequence of the one-year probability wave. The results indicate that the foreshore sands were lost due to surface erosion and scour in front of the base of the retaining wall. Under the continued action of the one-year probability wave, the internal erosion progressed beneath and behind the retaining wall, and collapse occurred. The extent of the collapse, however, was significantly smaller than the extent of collapse under the five-year probability wave that accompanied overtopping (Fig. 12(a)). Fig. 12(b) shows the situation of collapse in the absence of overtopping under the one-year probability wave.

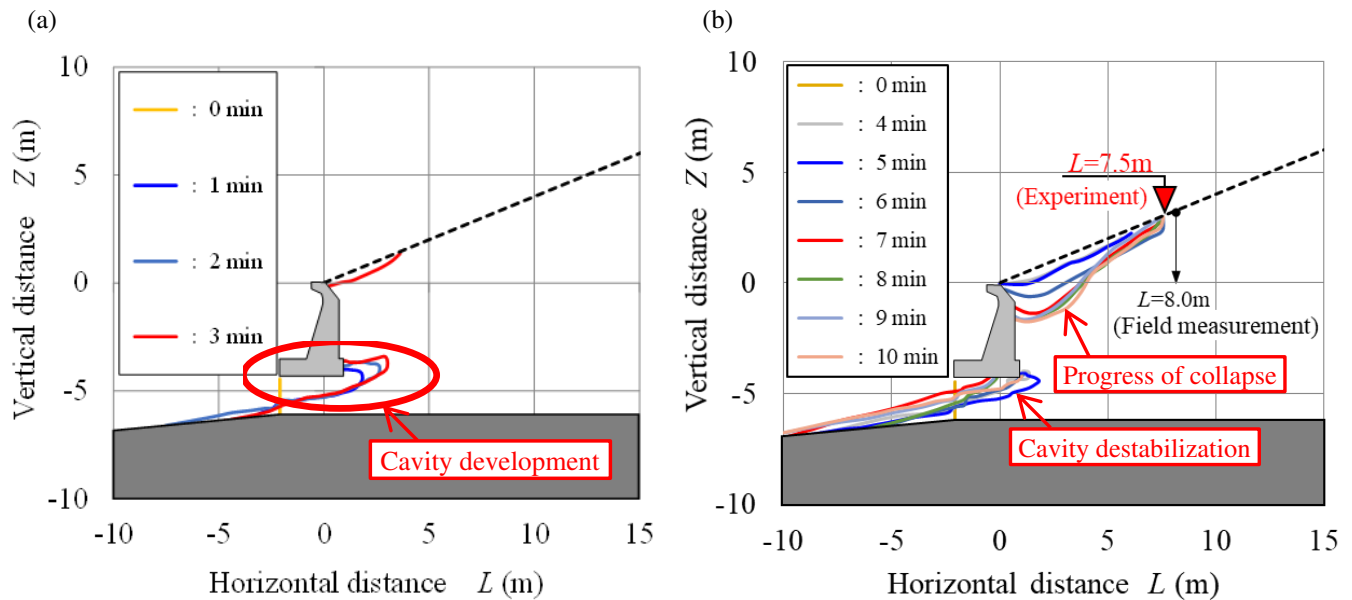


Figure 10. Results of the wave flume experiment for the 2014 disaster. Progress of internal erosion and collapse beneath/behind the retaining wall at: (a) 0 to 3 minutes, and (b) 4 to 10 minutes after the start of the experiment. Contours of deformations on a prototype scale.

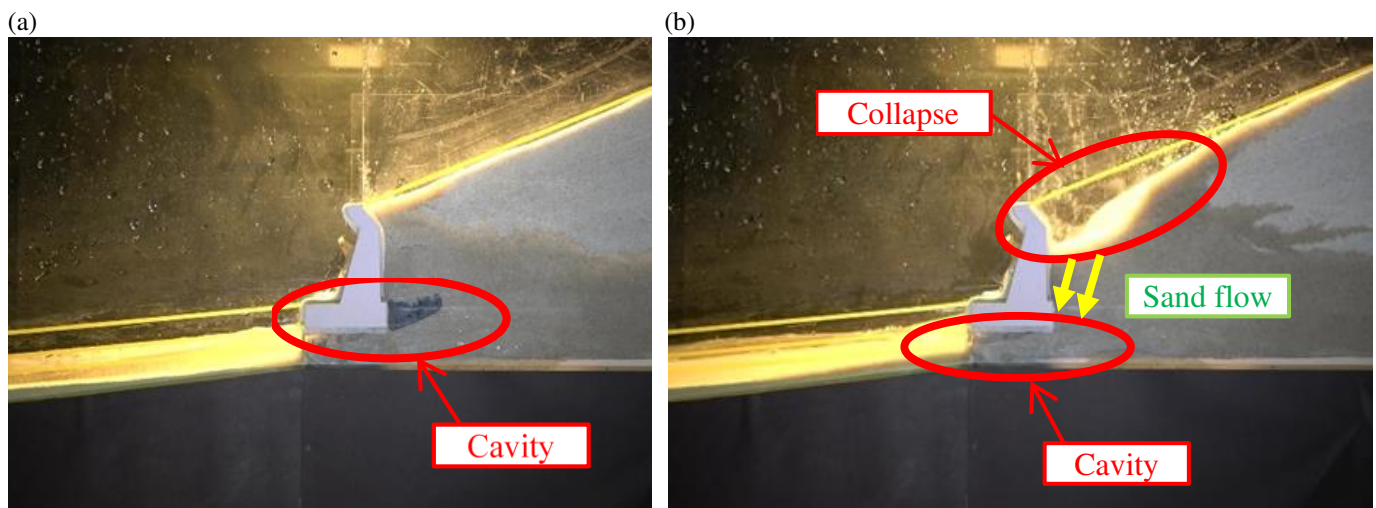


Figure 11. Results of the wave flume experiment for the 2014 disaster. Progress of internal erosion and collapse beneath/behind the retaining wall at: (a) 0 to 3 minutes, and (b) 4 to 10 minutes after the start of the experiment. Photographs.

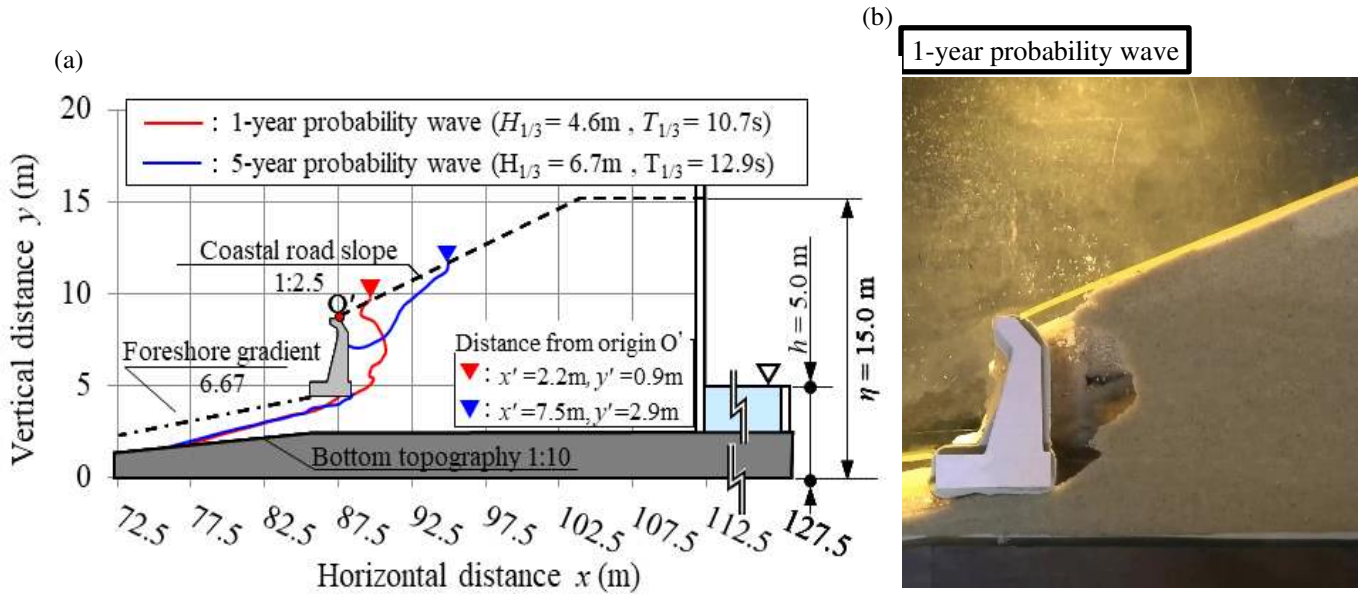


Figure 12. Results of the wave flume experiment for the 2021 disaster: (a) Comparison of deformations on a prototype scale beneath/behind the retaining walls under 1-year and 5-year probability waves, and (b) Collapse behind the retaining wall under 1-year probability waves.

Discussion on the Processes and Mechanisms for the 2014 and 2021 Disasters

The processes and mechanisms for the 2014 and 2021 disasters based on the field, numerical, and experimental investigations described above can be schematically shown in Fig. 13. For the 2014 disaster, the five-year probability wave produced wave overtopping. The wave-induced runup and return flow, i.e., swash and backwash, acted on the foreshore sands and the weak erodible bedrock. These caused surface erosion and scour in front of the base of the retaining wall. The continued severe wave action then gave rise to the occurrence of progressive internal erosion, accompanied by the formation of cavities beneath and behind the retaining wall. In the meantime, the wave overtopping/overflow led to erosion of the road slope surface behind the top of the wall. Here, the overflow represents infiltration that reduces suction in the ground, which has been shown to destabilize cavities formed by the wave-induced internal erosion (Kudai et al., 2021), and the overflow promotes flow-out of granular materials beneath a foundation of coastal structures (Sassa et al., 2016). Hence, the coupled severe wave action and overflow brought about subsidence and sand flow-out that resulted in a large collapse behind the retaining wall.

In contrast, the 2021 disaster stemmed from the one-year probability wave that did not produce wave overtopping. Nevertheless, the wave-induced runup and return flow, i.e., swash and backwash, were severe enough to cause surface erosion and scour in front of the base of the retaining wall, which gave rise to progressive internal erosion beneath and behind the retaining wall. The continued wave actions involving swash and backwash destabilized the cavities formed, leading to subsidence and sand flow-out. As a consequence, collapse occurred behind the retaining wall. Overall, both the 2014 and 2021 disasters share the same basic mechanisms: namely, the coupled surface erosion, scour, and internal erosion beneath and behind the retaining wall, which led to collapse. The existence of the overtopping flow enlarged the extent of collapse in the 2014 disaster compared to the 2021 disaster.

The above results and discussion indicate that the 2014 and 2021 disasters stemmed from the wave-induced internal erosion beneath and behind the retaining wall. This means that the deterrence of the internal erosion beneath the base of the retaining wall may serve as an effective countermeasure to prevent the occurrence of future collapse behind the retaining wall. This can be achieved by applying an appropriately designed filter, which has been shown to have a sufficient deterrent effect under strong hydraulic forcing at coasts (Kudai et al., 2021). Deterring the wave-induced internal erosion beneath the base of the retaining wall should thus be a viable measure, which could be conducted in conjunction with a protection work to suppress the influence of overtopping on the coastal road slope surface behind the retaining wall.

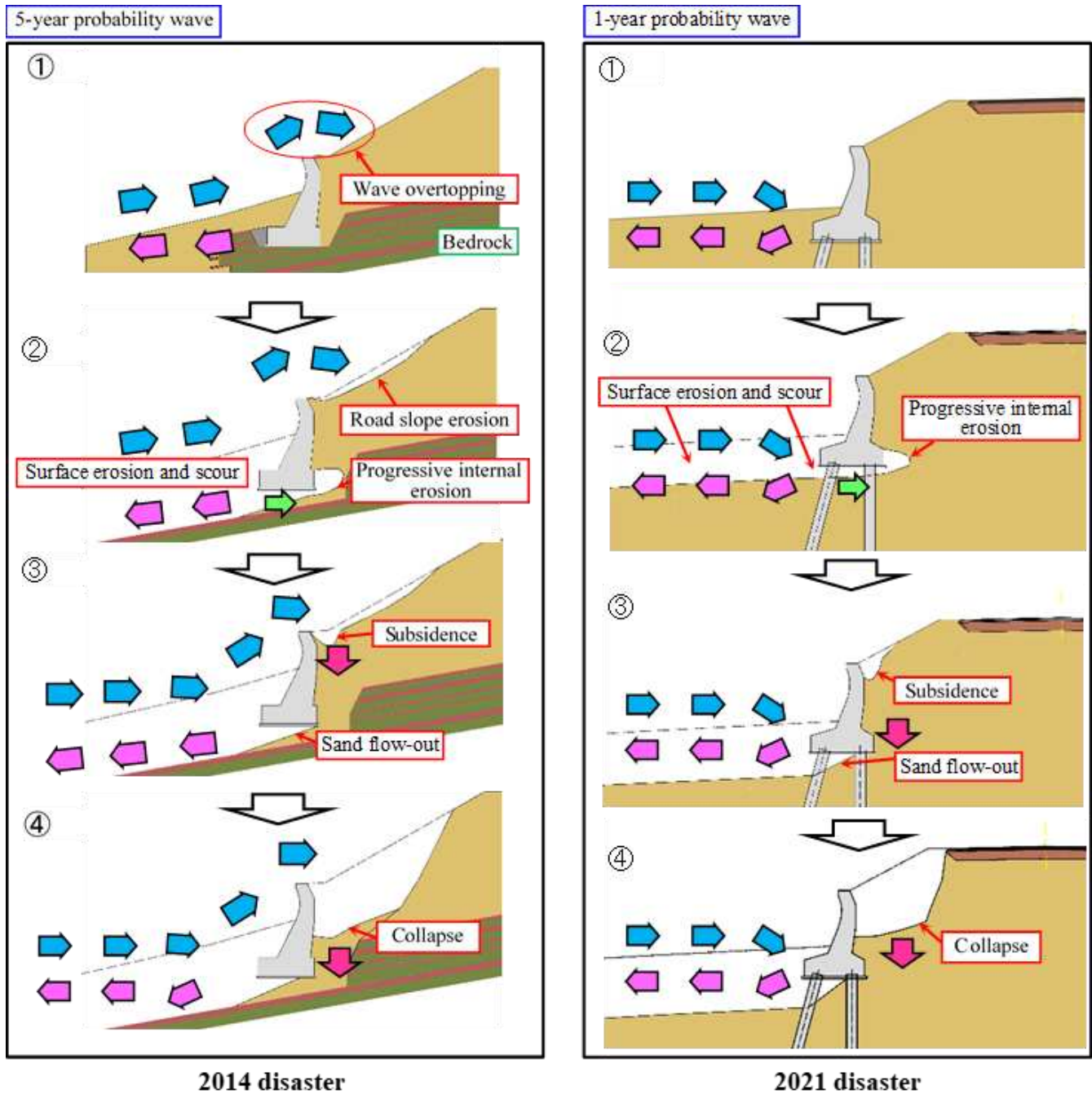


Figure 13. Schemes based on the field, numerical, and experimental investigations, showing the processes and mechanisms of the 2014 and 2021 disasters.

CONCLUSION

The results of the field surveys of the 2014 and 2021 disasters, combined with the analyses of wind waves and the hydraulic wave flume experiments, demonstrated the mechanisms for the collapses of the coastal road embankment slopes due to coupled surface erosion, scour, and internal erosion subject to waves, flows, and overtopping. The presence of overtopping enlarged the extent of collapses, whereas the simultaneous surface erosion and internal erosion beneath and behind the retaining walls led to collapses irrespective of overtopping. Hence, preventing erosion beneath the retaining wall through an appropriately designed filter may serve as an effective countermeasure for such coastal embankment slope collapse disasters.



REFERENCES

- Booij, N., Ris, R.C., and Holthuijsen, L.H. (1999). "A third-generation wave model for coastal regions: 1. Model description and validation." *Journal of Geophysical Research-Atmospheres*, 104(C4), 7649–7666.
- Bretschneider, C.L. (1968). *Significant waves and wave spectrum*, In Ocean Industry; Gulf Publishing Company: Houston, TX, USA.
- General Bathymetric Chart of the Oceans (GEBCO). "GEBCO_2020 grid." <<https://download.gebco.net/>>.
- Kudai, K., Sassa, S., Yang, S., and Takada, K. (2021). "Influence of soil and hydraulic conditions on the processes of internal erosion, cavity formation and collapse behind coastal structures." *Coastal Engineering*, 170, 104013.
- Mitsuyasu, H. (1970). "On the Growth of Wind-Generated Waves (2)—Spectral Shape of Wind Waves at Finite Fetch." Proc. of the 17th Japanese Conference, Kyoto, Japan.
- Morim, J., Hemer, M., Wang, X.L. Cartwright, N., Trenham, C., Semedo, A., Young, I., Bricheno, L., Camus, P., Casas-Prat, M., Erikson, L., Mentaschi, L., Mori, N., Shimura, T., Timmermans, B., Aarnes, O., Breivik, O., Behrens, A., Dobrynin, M., Menendez, M., Staneva, J., Wehner, M., Wolf, J., Kamranzad, B., Webb, A., Stopa, J., and Andutta, F. (2019). "Robustness and uncertainties in global multivariate wind-wave climate projections." *Nature Climate Change*, 9, 711–718.
- Nationwide Ocean Wave information network for Ports and HARbourS (NOWPHAS). <https://www.mlit.go.jp/kowan/nowphas/index_eng.html>.
- Ris, R.C., Holthuijsen, L.H., and Booij, N. (1999). "A third-generation wave model for coastal regions: 2. Verification." *Journal of Geophysical Research-Atmospheres*, 104(C4), 7667–7681.
- Sassa, S., Takahashi, H., Morikawa, Y., and Takano, D. (2016). "Effect of overflow and seepage coupling on tsunami-induced instability of caisson breakwaters." *Coastal Engineering*, 117, 157–165.
- SWAN Team. (2006). *SWAN Cycle III version 40.51 Technical documentation*, Delft University of Technology, Faculty of Civil Engineering and Geosciences, Environmental Fluid Mechanics Section, P.O.Box 5048, 2600 GA Delft, The Netherlands.
- Yang, Y., Gao, S., Wang, Y.P., Jia, J., Xiong, J., and Zhou, L. (2019). "Revisiting the problem of sediment motion threshold." *Continental Shelf Research*, 187, 103960.



INTERNATIONAL JOURNAL OF GEOENGINEERING CASE HISTORIES

*The Journal's Open Access Mission is
generously supported by the following Organizations:*



Access the content of the *ISSMGE International Journal of Geoengineering Case Histories* at:
www.geocasehistoriesjournal.org